

Machine-learning-based nonlinear decomposition of CT images for metal artifact reduction

Hyung Suk Park*, Sung Min Lee†, Hwa Pyung Kim†, and Jin Keun Seo†

* Division of Strategic Research, National Institute for Mathematical Sciences, Daejeon, 34047, South Korea

† Department of Computational Science and Engineering, Yonsei University, Seoul, 120-749, South Korea

Abstract—Computed tomography (CT) images containing metallic objects commonly show severe streaking and shadow artifacts. Metal artifacts are caused by nonlinear beam-hardening effects combined with other factors such as scatter and Poisson noise. In this paper, we propose an implant-specific method that extracts beam-hardening artifacts from CT images without affecting the background image. We found that in cases where metal is inserted in the water (or tissue), the generated beam-hardening artifacts can be approximately extracted by subtracting artifacts generated exclusively by metals. We used a deep learning technique to train nonlinear representations of beam-hardening artifacts arising from metals, which appear as shadows and streaking artifacts. The proposed network is not designed to identify ground-truth CT images (i.e., the CT image before its corruption by metal artifacts). Consequently, these images are not required for training. The proposed method was tested on a dataset consisting of real CT scans of pelvises containing simulated hip prostheses. The results demonstrate that the proposed deep learning method successfully extracts both shadowing and streaking artifacts.

Index Terms—Computerized tomography, Metal artifact reduction, Beam hardening, Deep learning.

I. INTRODUCTION

X-ray computed tomography (CT) provides tomographic images of the human body by assigning an X-ray attenuation coefficient to each pixel, using sinogram data (i.e., X-ray data collected at all angles around the object). The reconstruction methods used for CT images are based on a linear assumption of the sinogram data: namely, the Radon transform of an image. However, this assumption of linearity is violated in the presence of highly attenuating materials such as metal implants (e.g., hip replacements, dental fillings, surgical clips, and pacemaker wires) in the CT scan field. These discrepancies in the linear model are mainly caused by beam-hardening effects, which are associated with the polychromatic nature of the X-ray beam and the energy-dependent variations in the attenuation coefficients of highly attenuating materials. The inconsistent sinogram data attributable to these beam-hardening effects do not match the Radon transform of any attenuation coefficient distribution. Consequently, metallic artifacts seriously degrade the CT images of patients with metal implants.

Because metallic implants are increasingly popular, there is a growing demand for metal artifact reduction (MAR) in dentistry and medicine. Despite numerous efforts to develop

MAR methods in the last four decades, it remains a very challenging problem because of the difficulties presented by the nonlinear effects that arise from the geometry of high-attenuation materials, polychromatic X-ray beams, and related artifacts, together with Compton scattering, photon noise, and so on. Existing MAR methods include dual-energy CT [1], statistical iterative-reconstruction methods [6], [7], [18], [21], [30], data completion/inpainting-based methods [3], [12], [16], [19], [22], [24], [27], and hybrid methods [15]. However, several current methods produce new artifacts that are not present before the application of the method [19], [20].

In this paper, we propose a deep learning method for implant-specific MAR that extracts beam-hardening artifacts from CT images. In cases where metal inserts are placed inside of tissue (or water), we found that metal-induced beam-hardening artifacts can be approximately extracted by subtracting artifacts generated exclusively by metal inserts. With this observation, the proposed MAR method takes advantage of training with metal-only images to extract features of the beam-hardening artifacts.

Because beam-hardening artifacts depend on the metal geometry, energy dependency of the attenuation coefficient, and the spectrum of the incident X-ray beam, the number of variations is too great to allow the features to be learned. This obstacle is dealt with by incorporating prior knowledge of the geometry of the metallic objects. Indeed, the geometry and material information of implants such as hip replacements and endovascular stents are usually known. With this knowledge of the scanned metal, we adopt a multi-scale convolutional network, called U-net [28], to train the model using metal-only images.

In the presence of metallic objects, no ground-truth CT images (i.e., CT images before corruption by metal artifacts) are available. In such cases, they cannot be used as label data for learning. The proposed method does not require ground-truth image, insofar as it learns artifacts generated exclusively by metal, rather than artifact-free CT images.

We explore the feasibility of applying a deep learning approach to MAR using a dataset consisting of real CT scan of pelvises containing two simulated hip prostheses. The results demonstrate that the proposed deep learning method successfully extracts both shadowing and streaking artifacts.

II. METHOD

Considering a two-dimensional parallel beam, we define X-ray data for a polychromatic X-ray along the rotation direction

$(\cos \varphi, \sin \varphi)$, $\varphi \in [0, 2\pi)$ as

$$P_f(\varphi, s) = -\ln \left(\int_0^{\bar{E}} \eta(E) e^{-\mathcal{R}f_E(\varphi, s)} dE \right), \quad (1)$$

where $f_E(\mathbf{x})$ denotes the distribution of the attenuation coefficient at position $\mathbf{x} = (x_1, x_2)$ and at energy level E , $\eta(E)$ represents the fractional energy at photon energy E in the spectrum of the X-ray source [11], [25], that is, $\int_0^{\bar{E}} \eta(E) dE = 1$, and \mathcal{R} denotes the Radon transform [26]. The most widely used reconstruction method for CT is the filtered backprojection algorithm (FBP):

$$f_{\text{CT}}(\mathbf{x}) := \mathcal{R}^{-1} P_f(\mathbf{x}), \quad (2)$$

where \mathcal{R}^{-1} denotes the filtered backprojection operator [4].

Artifact

In this section, we propose a method of extracting beam-hardening artifacts arising from metallic objects from the measured f_{CT} . Let the cross-sectional slice to be scanned occupy a domain Ω . Assume that f_E can be expressed as

$$f_E(\mathbf{x}) = \mu_t(E)\chi_{D_t}(\mathbf{x}) + \mu_m(E)\chi_{D_m}(\mathbf{x}), \quad \mathbf{x} \in \Omega, \quad (3)$$

where μ_t and μ_m denote the linear attenuation coefficients of tissue and the metal in the domain D_t , $D_m \subset \Omega$, respectively. Here, χ_D denotes the characteristic function, which is 1 in the region D and 0, otherwise. Let P_{f^m} , P_{f^t} be the projection data for metal and tissue given by

$$P_{f^m}(\varphi, s) = -\ln \left(\int_0^{\bar{E}} \eta(E) e^{-\mu_m(E)\mathcal{R}\chi_{D_m}(\varphi, s)} dE \right), \quad (4)$$

and

$$P_{f^t}(\varphi, s) = -\ln \left(\int_0^{\bar{E}} \eta(E) e^{-\mu_t(E)\mathcal{R}\chi_{D_t}(\varphi, s)} dE \right), \quad (5)$$

respectively. Let f^m and f^t be the CT images for P_{f^m} and P_{f^t} , respectively. The following observation expresses the extraction of metal artifacts (f^m) from f_{CT} (see also Fig.1):

Observation 2.1: Let D_m be a homogeneous metal region inserted in the tissue. Then, the f_{CT} in (2) can be approximately decomposed into

$$f_{\text{CT}}(\mathbf{x}) \approx \tau\chi_{D_m}(\mathbf{x}) + f^t(\mathbf{x}) + \gamma f^m(\mathbf{x}), \quad (6)$$

where τ, γ are the constants depending on the distribution of μ_m and μ_t . In the absence of tissue, that is, $f^t(\mathbf{x}) = 0$, for all $\mathbf{x} \in \Omega$, $\tau = 0$ and $\gamma = 1$.

Figure 1 illustrates Observation 2.1. Fig. 1(a) shows a phantom consisting of water and two cylinders filled with highly attenuating fluid. The fluid consists of iodinated contrast media and saline. Fig. 1(b) shows the corresponding f_{CT} obscured by artifacts arising from this fluid. Figs. 1(c) and (d) show f^m and $f_{\text{CT}} - \gamma f^m$ with $\gamma = 0.4$, respectively. Fig. 1(d) shows that the beam-hardening artifacts are almost completely removed from f_{CT} . In addition, because f^m is subtracted from f_{CT} , streaking artifacts due to under-sampling are significantly reduced. In this experiment, CT images were acquired from

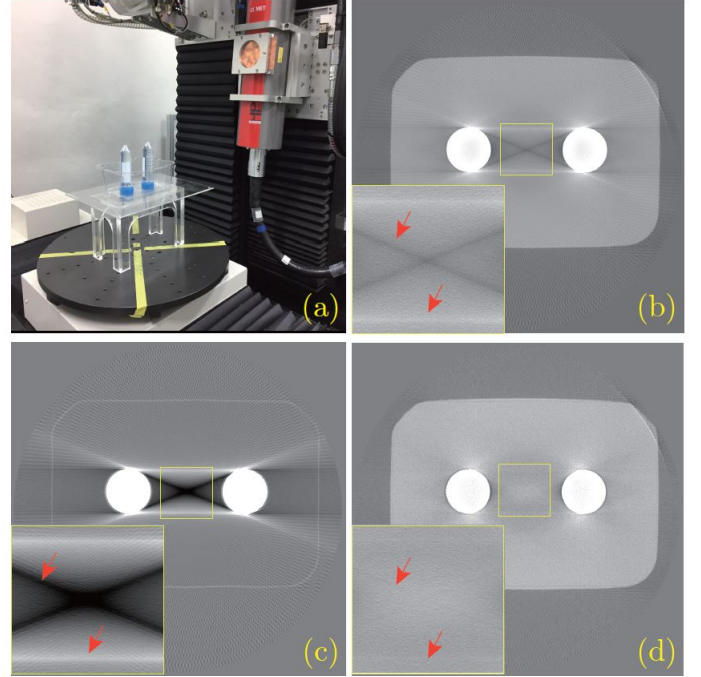


Fig. 1. Illustration of Observation 2.1: (a) water phantom consisting of water and two cylinders filled with highly attenuating fluid; (b) reconstructed image f_{CT} ; (c) metal-induced artifact f^m ; and (d) $f_{\text{CT}} - \gamma f^m$ with $\gamma = 0.4$. ($C=1000$ HU/ $W=4000$ HU for CT images.)

an industrial CT scanner (DUKIN, Korea) with an X-ray tube voltage of 100 kV and a tube current of 12 mA.

Now, let us discuss the meaning of Observation 2.1. Equation (6) implies that for all X-rays passing through metallic objects, two μ_m at mean beam energies in the presence and absence of tissue have a nearly-linear relationship. More specifically, the projection data corresponding to (6) is given by

$$P_f(\varphi, s) \approx \tau\mathcal{R}\chi_{D_m}(\varphi, s) + P_{f^t}(\varphi, s) + \gamma P_{f^m}(\varphi, s). \quad (7)$$

Because $\int_0^{\bar{E}} \eta(E) dE = 1$, it follows from the mean value theorem for integration that for each $(\varphi, s) \in [0, 2\pi) \times \mathbb{R}$, there exists $E_{\varphi, s}^c, E_{\varphi, s}^m \in [0, \bar{E}]$, such that

$$\begin{aligned} & \int_0^{\bar{E}} \eta(E) e^{-\mu_m(E)\mathcal{R}\chi_{D_m}(\varphi, s) - \mu_t(E)\mathcal{R}\chi_{D_t}(\varphi, s)} dE \\ &= e^{-\mu_m(E_{\varphi, s}^c)\mathcal{R}\chi_{D_m}(\varphi, s)} \int_0^{\bar{E}} \eta(E) e^{-\mu_t(E)\mathcal{R}\chi_{D_t}(\varphi, s)} dE \end{aligned} \quad (8)$$

and

$$\int_0^{\bar{E}} \eta(E) e^{-\mu_m(E)\mathcal{R}\chi_{D_m}(\varphi, s)} dE = e^{-\mu_m(E_{\varphi, s}^m)\mathcal{R}\chi_{D_m}(\varphi, s)}. \quad (9)$$

It follows from (8) and (9) that (7) can be expressed as

$$\mu_m(E_{\varphi, s}^c)\mathcal{R}\chi_{D_m}(\varphi, s) \quad (10)$$

$$\approx \tau\mathcal{R}\chi_{D_m}(\varphi, s) + \gamma \mu_m(E_{\varphi, s}^m)\mathcal{R}\chi_{D_m}(\varphi, s). \quad (11)$$

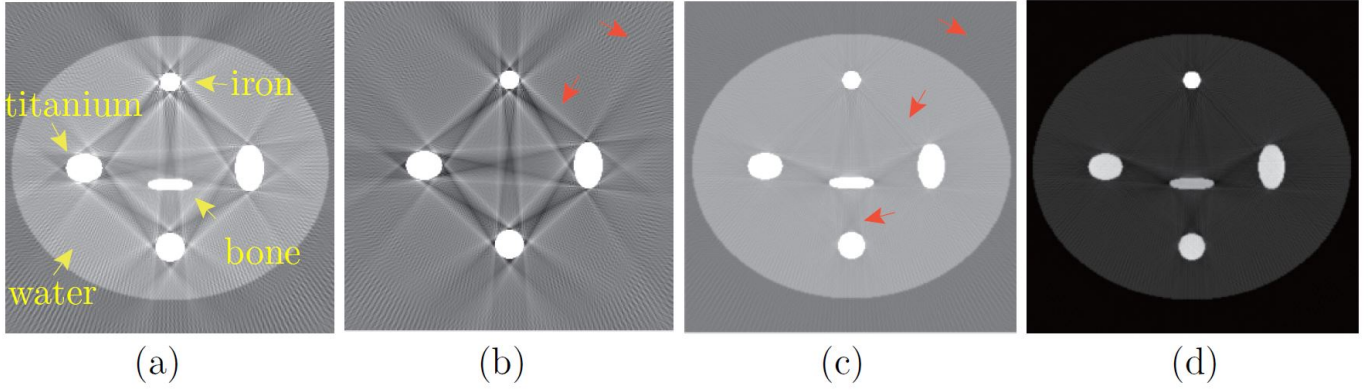


Fig. 3. Results from extracting metal-induced beam-hardening artifacts. Figures (a) and (b) show f_{CT} for a water phantom containing four metallic inserts (three titanium and one iron) and f^m , respectively. Figures (c) and (d) show $f_{CT} - \gamma f^m$ with $\gamma = 0.74$ at different window levels. ($C=500$ HU/ $W=3000$ HU for (a), (b) and (c), and $C=2500$ HU/ $W=6000$ HU for (d).)

by a rectified linear unit (ReLU), along with 2×2 max pooling with strides of two in each direction of the domain. In each step of the expansive path, the average unpooling is used instead of max pooling. Then, it is concatenated with the features in the contracting path during the same step. Note the every convolution in our network is performed with zero-padding in order to match the size of the input and label images.

C

The proposed method is based on the following steps (see also Fig. 4):

- (i) From the measured P_f , reconstruct the uncorrected f_{CT} using the FBP algorithm.
- (ii) Generate g^m from the formula (15), and then generate the output \tilde{f}^m from the trained network.
- (iii) Compute corrected CT image $f_{CT} - \gamma \tilde{f}^m$.

In Step (ii), g^m in (15) is determined by the region D_m and parameters λ and c , which are obtained by the following procedure. First, the D_m is extracted with simple thresholding from f_{CT} , and λ is determined as in [23]. From the relation of (15) and $f^m \approx g^m$, c is computed as follows:

$$c = \frac{1}{|X_{D_m}|} \int_{D_m} f^m(\mathbf{x}) + \mathcal{R}^{-1} \left[\ln \left(\frac{\sinh(\lambda \mathcal{R} X_{D_m})}{\lambda \mathcal{R} X_{D_m}} \right) \right] (\mathbf{x}) d\mathbf{x}. \quad (17)$$

Here, c is computed as the average value over D_m . In Step (iii), we determine γ in such a way that any streaking artifacts arising from metals are alleviated in $f_{CT} - \gamma \tilde{f}^m$. More specifically, we find the γ minimizing the function Φ given by

$$\Phi(\gamma) = \int_{\Omega \setminus D_m} |\nabla(f_{CT}(\mathbf{x}) - \gamma \tilde{f}^m(\mathbf{x}))|^2 d\mathbf{x}. \quad (18)$$

Because $\Phi(\gamma)$ is one-dimensional function with respect to γ , one can easily find minimizer γ by computing $\Phi(\gamma)$ over the suitable interval.

Note that the error $g^m - f^m$ comes from model's assumption used to derived the formula g^m , for example, from the use of a linear approximation for nonlinear variation in the attenuation coefficient [23] (see Fig. 4).

III. RESULTS

A

In general, deep learning methods require a considerable amount of training data. However, it is very difficult to obtain large amounts of real training data for MAR. We show the feasibility of applying a deep learning approach to MAR by using numerical simulations with real data. The proposed method was tested on real CT images of pelvises containing two simulated metallic (iron) inserts. In our simulations, P_f and P_{f_m} in (1) and (4) were generated with an X-ray tube voltage of 100 kV with added Poisson noise. We used η for the tungsten anode generated at a tube voltage of 100 kVp [5]. Other causes of metal artifacts, such as scattering and nonlinear partial volume effects were not considered. Here, f_{CT} and f^m were acquired by applying FBP to P_f and P_{f_m} , respectively. We took f^m as the label. The input image g^m was generated from (15). Note that λ and c in (15) are associated with the η and μ_m of metallic materials. Hence, we used fixed λ and c for all input g^m . To train our network, we generated 690 CT images for two metallic objects in a symmetric position around the origin by changing their shape and position. More specifically, let $(\theta, r, (a_1, b_1, a_2, b_2))$ be a pair of transformation parameters for metallic objects to determine the shape and position. Here, θ denotes the rotation angle around the origin, r is the distance from the origin to center of the metal, and $(a_1, b_1), (a_2, b_2)$ denotes the pair of semi-major and semi-minor axes of the ellipse for each metal. We selected $\theta = (-43^\circ, -39^\circ, \dots, 45^\circ)$, $r = (7cm, 9cm, \dots, 15cm)$, and $(a_1, b_1, a_2, b_2) = (2, 2, 2, 2), (3, 3, 3, 3), (4, 4, 4, 4), (1, 2, 2, 1), (2, 3, 3, 2), (3, 4, 4, 3)$, with an image size of 50×50 cm (see Fig. 5). For the test images, we generated CT images for a simulated hip prosthesis, with geometry similar to the training set, obtained from pelvis CT images.

B

The error (16) was minimized using the RMSPropOptimizer [29] with a learning rate of 0.001, weight decay of 0.9, and mini-batch size of 20. We used 200 epochs to train the

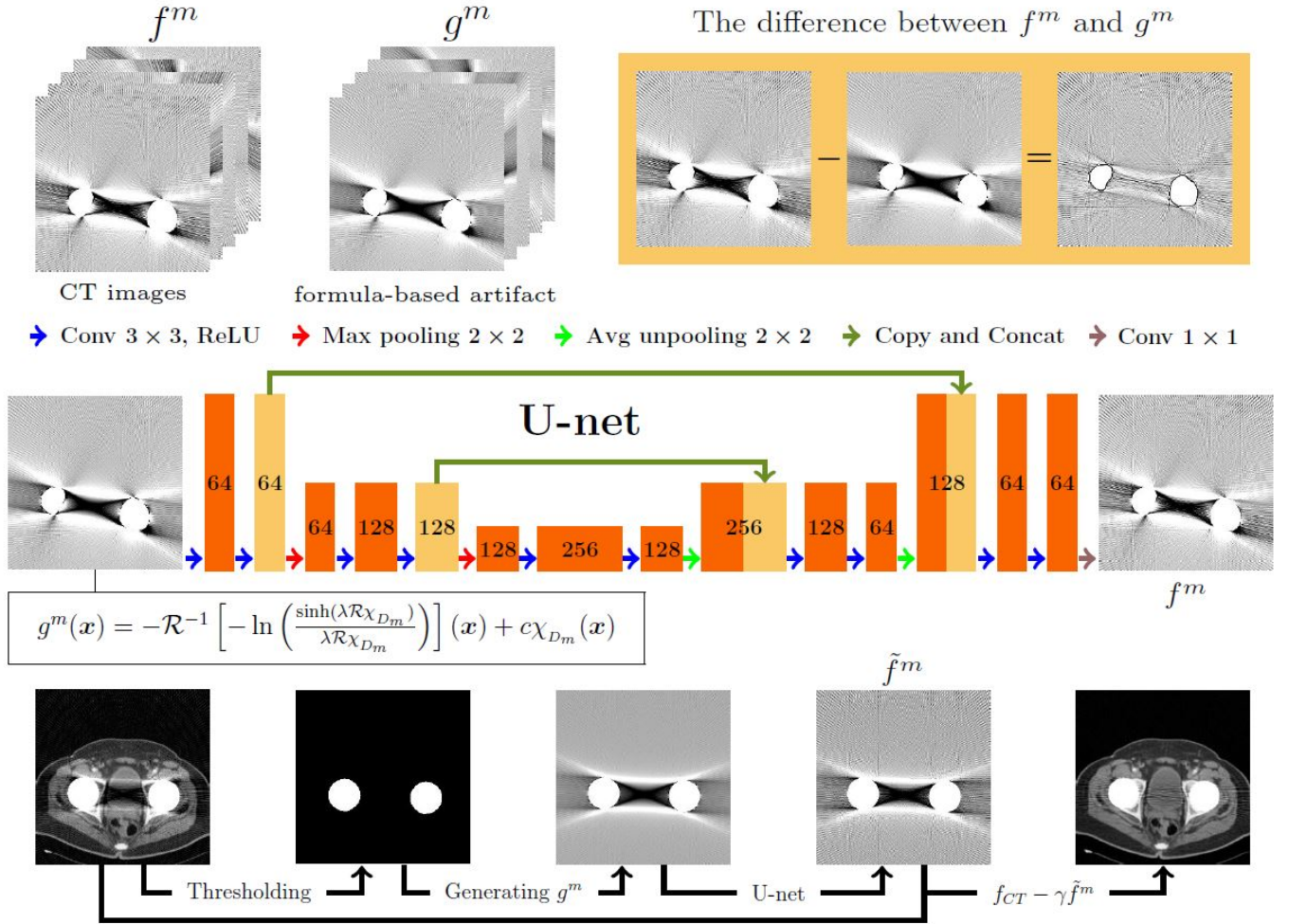


Fig. 4. Illustration of the multi-scale convolutional network for training f^m from g^m , along with the algorithm for the proposed method.

network. Training was implemented by Tensorflow [8] on a CPU (Intel(R) Core(TM) i7-6850K, 3.60GHz) and a GPU (NVIDIA GTX-1080, 8GB) system. It required approximately one hour to train our network.

CMR

Fig. 5 shows a manifold \mathcal{M} of CT metal-artifact images, which can be viewed as a set of points in high-dimensional space $\mathbb{R}^{256 \times 256}$ with 256×256 pixel CT images. Because linear combinations of two images on \mathcal{M} do not resemble metal-induced beam-hardening artifacts, \mathcal{M} is unlike Euclidean space. Our trained network performed well in terms of both the test set and training set. In other words, the regression manifold \mathcal{M} effectively interpolated between CT metal artifact images in terms of their trajectories, as shown in Fig. 5. Although we use a relatively small training data, the network produced reasonably accurate metal artifacts that were not in the training set. Fig. 6 depicts the L^2 error and test image results with respect to the number of epochs. It shows that the L^2 error converged and that beam-hardening artifacts in test image were reduced as the number of epochs increased.

Fig. 7 shows the numerical simulation results for MAR. The first and second columns show the reference and f_{CT} , respec-

tively. The third and fourth columns represent the correction results using MAC-BC and the proposed method, respectively. MAC-BC [23] extracts beam-hardening artifacts from f_{CT} based on an analytic formula. Both correction methods show that the anatomical information corrupted by beam-hardening effects is clearly visible. However, MAC-BC still retained some streaking artifacts, owing to model's assumption of linear approximation for nonlinear variations (see Fig. 7, third column). By comparison, the proposed method outperformed MAC-BC in terms of beam-hardening artifact reduction (see Fig. 7, fourth column). In order to compare the quantitative errors in the corrected image (f_{cor}) from each method with those of the reference image (f_{ref}), we computed the normalized root mean square difference (NRMSD) [17] on the outside of D_m . The NRMSD (%) for each result is listed in Table I. The proposed method obtained the lowest NRMSD in all cases. This shows that the proposed method performs better at background restorations.

IV. DISCUSSION AND CONCLUSION

We developed a deep learning MAR method to extract streaking and shadow artifacts from artifact-contaminated CT images arising from the presence of metallic objects. We

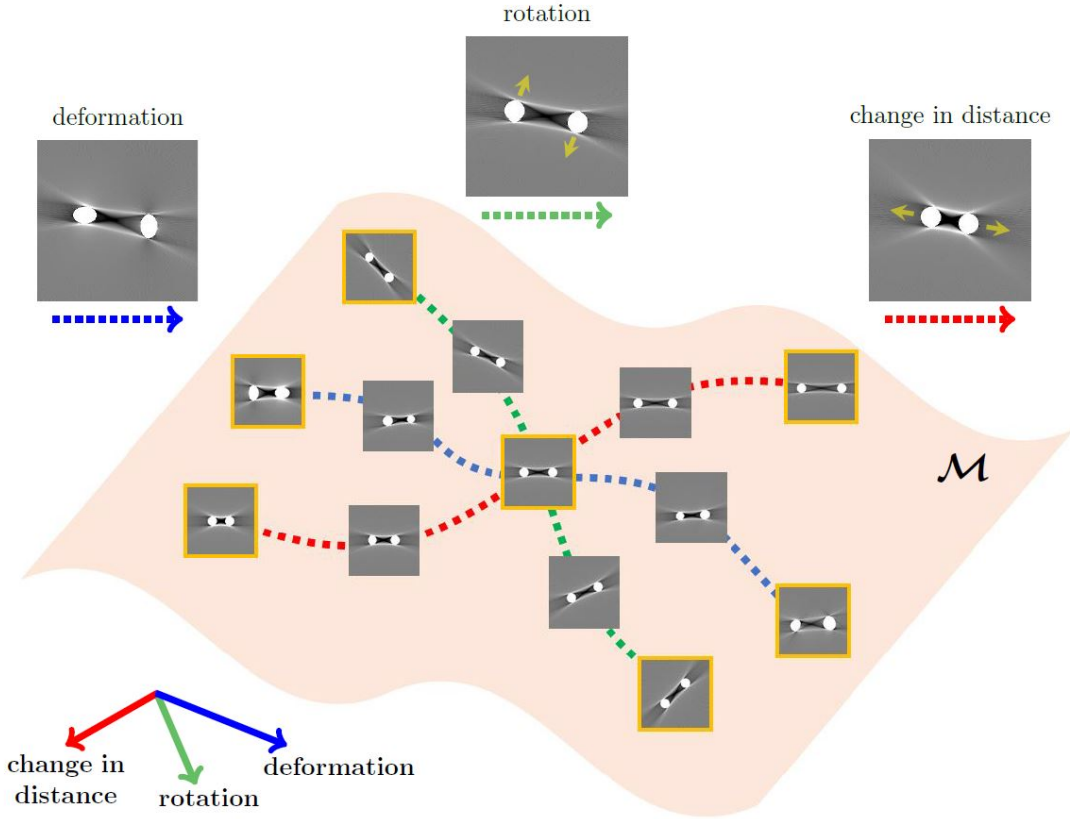


Fig. 5. Manifold of CT metal-artifact images. The trajectories in the embedding correspond roughly to smooth variations in metal artifacts with respect to rotation, deformation, and distance.

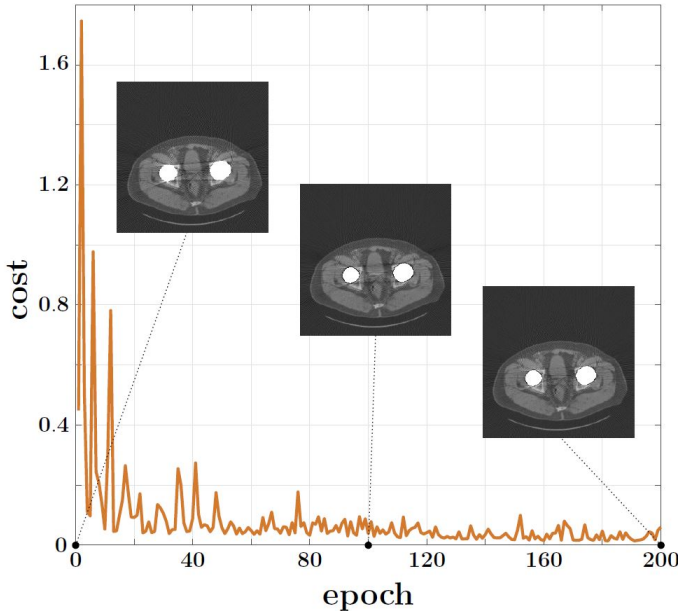


Fig. 6. Convergence plot for the L^2 error and test image results with respect to the number of epochs.

demonstrated that the proposed method effectively provides nonlinear representations of shadows and streaking artifacts attributable to metallic objects. Ex-vivo features of metal

TABLE I
NRMSD OF THE RECONSTRUCTED IMAGE WITH THE MAC-BC METHOD AND THE PROPOSED METHOD

	Phantom	Uncorrected	MAC-BC	Proposed
NRMSD	Pelvis 1	54.67	21.10	14.67
	Pelvis 2	46.68	18.95	13.60
	Pelvis 3	65.83	26.68	16.43
	Pelvis 4	46.87	24.96	16.87

artifacts were used for training rather than real in-vivo features, because there are no available ground-truth CT images for deep learning.

The proposed method works well with a relatively small number of training images, despite numerous variations to these artifacts in terms of the metal shape and placement. We took advantage of the observation that metal-induced artifacts can be determined approximately from variations in metal geometry with respect to rotation, deformation, and distance. Hence, the collection of CT images of metal artifacts can be assumed to lie on a low-dimensional submanifold \mathcal{M} embedded in high-dimensional space R^N , with the dimension N denoting the number of pixels in the CT images. This observation allowed us to reduce the size of the training set significantly, with interpolation over the trajectory as shown in Fig. 5.

However, there is room to further improve this method. The extraction procedure for metal artifacts could be modified

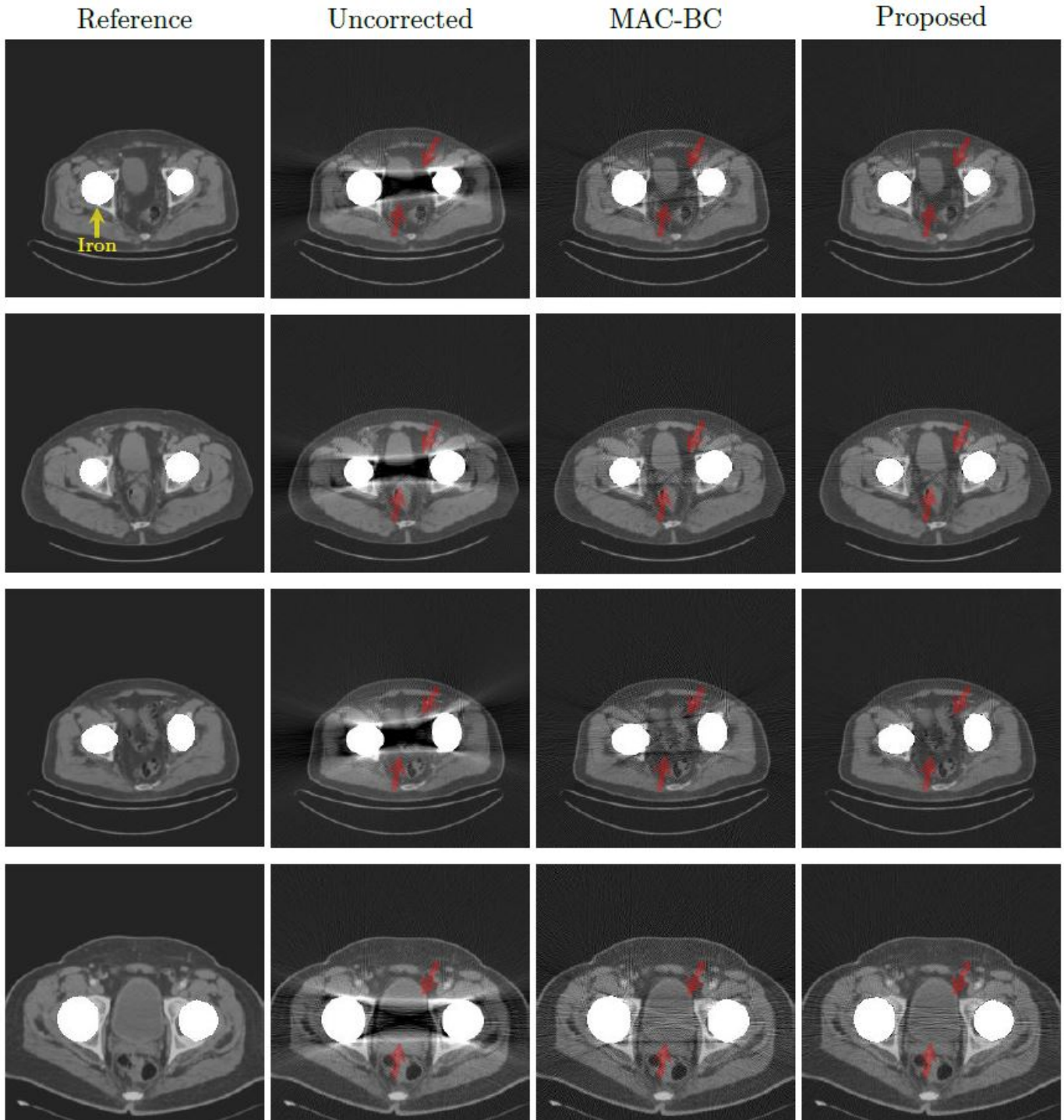


Fig. 7. Illustration of the numerical simulation results. The first and second columns show the reference and uncorrected image, respectively. The third and fourth columns represent the results with MAC-BC and the proposed method, respectively. The red arrows in the images mark the position of the artifacts. The results show that the proposed method reduce streaking artifacts more clearly than the MAC-BC method. ($C=1000$ HU/ $W=3000$ HU.)

by enhancing the forward model, which accurately represents real artifacts arising exclusively from metal inserts. Based on Observation 2.1, these real artifacts could be extracted directly from CT images, without any deep learning process. Various experimental studies with patients will be required to explore the ability of this deep-learning-based approach, and we shall explore this in our future work.

ACKNOWLEDGEMENTS

The authors (S. M. Lee, H. P. Kim, and J. K. Seo) was supported by Samsung Science & Technology Foundation (No. SSTF-BA1402-01). The first author (H. S. Park) was partially supported by the National Research Foundation of Korea(NRF) grant funded by the Korea government(Ministry of Science, ICT & Future Planning) (No. NRF-2016RIC1B2008098) and the National Institute for Mathematical Sciences (NIMS) grant funded by the Korean government (No. A21300000).

REFERENCES

- [1] R. E. Alvarez and A. Macovski, Energy-selective reconstructions in X-ray computerised tomography, *IEEE Trans. Med. Imag.*, 21, pp. 733–1976.
- [2] J. F. Barrett, and N Keat, Artifacts in CT: recognition and avoidance, *Br. J. Radiol.*, 24, pp. 1679–1691, 2004.
- [3] M. Bazalova, L. Beaulieu, S. Palefsky, and F. Verhaegen, Correction of CT artifacts and its influence on monte carlo dose calculations, *Med. Phys.*, 34, pp. 2119–2132, 2007.
- [4] Bracewell RN, Riddle AC. Inversion of fan-beam scans in radio astronomy. *Astron. J.* 150. pp. 427, 1967.
- [5] J. Bushberg, J. Seibert, E. Leidholdt Jr, and J. Boone, *Essentials of Diagnostic Radiology*. Lippincott Williams & Wilkins, 2002.
- [6] B. De Man, J. Nuyts, P. Dupont, G. Marchal, and P. Suetens, An iterative maximum-likelihood polychromatic algorithm for CT, *IEEE Trans. Med. Imag.*, 20, pp. 999–1008, 2001.
- [7] I. A. Elbakri and J. A. Fessler, Statistical image reconstruction for polyenergetic X-ray computed tomography, *IEEE Trans. Med. Imag.*, 21, pp. 89–99, 2002.
- [8] Google. TensorFlow: Large-scale machine learning on heterogeneous systems, 2015. URL <http://tensorflow.org/>. Software available from tensorflow.org.
- [9] J. Gu, and J. C. Ye, Multi-Scale Wavelet Domain Residual Learning for Limited-Angle CT Reconstruction, arXiv preprint arXiv:1703.01382, 2017.
- [10] Y. Han, J. Yoo, and J. C. Ye, Deep residual learning for compressed sensing CT reconstruction via persistent homology analysis, arXiv preprint arXiv:1611.06391, 2016.
- [11] G. T. Herman and S. S. Trivedi, A comparative study of two postreconstruction beam hardening correction methods, *IEEE Trans. Med. Imag.*, 2, pp. 128–135, 1983.
- [12] W. A. Kalender, R. Hebel, and J. Ebersberger, Reduction of CT artifacts caused by metallic implants, *IEEE Trans. Med. Imag.*, 164, pp. 576–577, 1987.
- [13] Y. LeCun, B. Boser, J.S. Denker, D. Henderson, R.E. Howard, W. Hubbard, L.D. Jackel, Backpropagation applied to handwritten zip code recognition, *IEEE Trans. Neural Networks*, 1, pp. 541–551, 1989.
- [14] L. Lehmann, R. Alvarez, A. Macovski, W. Brody, N. Pelc, S. Riederer, and A. Hall, Generalized image combinations in dual kVp digital radiography, *IEEE Trans. Med. Imag.*, 8, pp. 659–667, 1981.
- [15] C. Lemmens, D. Faul, and J. Nuyts, Suppression of metal artifacts in CT using a reconstruction procedure that combines MAP and projection completion, *IEEE Trans. Med. Imag.*, 28, pp. 250–260, 2009.
- [16] R. M. Lewitt and R. H. T. Bates, Image reconstruction from projections: Iv: Projection completion methods (computational examples), *IEEE Trans. Med. Imag.*, 50, pp. 269–278, 1978.
- [17] A. Mehranian, M. R. Ay, A. Rahmim, and H. Zaidi, X-ray CT metal artifact reduction using wavelet domain sparse regularization, *IEEE Trans. Med. Imag.*, 32, pp. 1707–1722, 2013.
- [18] N. Menvielle, Y. Goussard, D. Orban, and G. Soulez, Reduction of beam-hardening artifacts in X-ray CT, *IEEE Trans. Med. Imag.*, 27, pp. 1865–1868.
- [19] E. Meyer, R. Raupach, M. Lell, B. Schmidt, and M. Kachelrieß, Normalized metal artifact reduction (NMAR) in computed tomography, *IEEE Trans. Med. Imag.*, 37, pp. 5482–5493, 2010.
- [20] J. Müller and T. M. Buzug, Spurious structures created by interpolation-based CT metal artifact reduction, *IEEE Trans. Med. Imag.*, 27, pp. 1Y1–1Y8.
- [21] J. A. O’Sullivan and J. Benac, Alternating minimization algorithms for transmission tomography, *IEEE Trans. Med. Imag.*, 26, pp. 283–297, 2007.
- [22] H. S. Park, J. K. Choi, K. R. Park, K. S. Kim, S. H. Lee, J. C. Ye, and J. K. Seo, Metal artifact reduction in CT by identifying missing data hidden in metals, *IEEE Trans. Med. Imag.*, 21, pp. 357–372, 2013.
- [23] H. S. Park, D. Hwang and J. K. Seo, “Metal artifact reduction for polychromatic X-ray CT based on a beam hardening corrector”, *IEEE Trans. Med. Imag.* vol.35, pp. 480–487, 2016.
- [24] M. Abdoli, M. R. Ay, A. Ahmadian, R. A. Dierckx, and H. Zaidi, Reduction of dental filling metallic artifacts in CT-based attenuation correction of PET data using weighted virtual sinograms optimized by a genetic algorithm, *IEEE Trans. Med. Imag.*, 37, pp. 6166–6177, 2010.
- [25] G. Poludniowski, G. Landry, F. DeBlois, P. Evans, and F. Verhaegen, Spekcalc: a program to calculate photon spectra from tungsten anode X-ray tubes, *Phys. Med. Biol.*, 54, pp. N433–N438, 2009.
- [26] J. Radon, “1.1 über die bestimmung von funktionen durch ihre integralwerte längs gewisser mannigfaltigkeiten”, *Classic papers in modern diagnostic radiology*, 5, (2005).
- [27] J. C. Roeske, C. Lund, C. A. Pelizzari, X. Pan, and A. J. Mundt, Reduction of computed tomography metal artifacts due to the fletcher-suit applicator in gynecology patients receiving intracavitary brachytherapy, *Int. J. Radiat. Oncol. Biol. Phys.*, 2, pp. 207–214, 2003.
- [28] O. Ronneberger, P. Fischer, and T. Brox, U-net: Convolutional networks for biomedical image segmentation, In *International Conference on Medical Image Computing and Computer-Assisted Intervention*, pp. 234–241, Springer, 2015.
- [29] T. Tieleman and G. Hinton, “Lecture 6.5-rmsprop: Divide the gradient by a running average of its recent magnitude”, COURSERA:Neural Networks for Machine Learning, 2012
- [30] G. Wang, D. L. Snyder, D. A. O’Sullivan, M. W. Vannier, Iterative deblurring for ct metal artifact reduction, *IEEE Trans. Med. Imag.*, 15, pp. 657–664, 1996